

## Activity and stability of powder and monolith-coated Ni/GDC catalysts for CO<sub>2</sub> methanation

Antonio Vita<sup>a,\*</sup>, Cristina Italiano<sup>a</sup>, Lidia Pino<sup>a</sup>, Patrizia Frontera<sup>b,c</sup>, Marco Ferraro<sup>a</sup>, Vincenzo Antonucci<sup>a</sup>

<sup>a</sup> CNR-ITAE "Nicola Giordano", Via Salita S. Lucia sopra Contesse 5, 98126, Messina, Italy

<sup>b</sup> Dept. of Civil Engineering, Energy, Environment and Materials (DICEAM), University "Mediterranea" of Reggio Calabria, Via Graziella, Feo di Vito, 89124, Reggio Calabria, Italy

<sup>c</sup> National Interuniversity Consortium of Materials Science and Technology (INSTM), Via G. Giusti 9, 50121, Firenze, Italy



### ARTICLE INFO

#### Keywords:

CO<sub>2</sub> methanation  
Ni catalysts  
Gadolinia doped ceria  
Structured catalyst  
Solution combustion synthesis

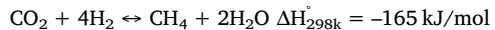
### ABSTRACT

The methanation of CO<sub>2</sub> via the Sabatier process is gaining interest for power-to-gas (P2G) application. In this work, CO<sub>2</sub> methanation activity and stability were investigated over Ni/GDC (gadolinium-doped-ceria) catalysts at atmospheric pressure varying reaction temperature (T<sub>SET</sub> = 300–600 °C) and space velocity (GHSV = 10,000–50,000 h<sup>-1</sup>). Powder catalysts with different Ni content (15–50 wt.%) were synthesized by the solution combustion synthesis (SCS). The same method was adopted to *in situ* deposit the Ni/GDC (50 wt.%Ni) coating layer on the cordierite monolith (500 cpsi). The catalysts were characterized by N<sub>2</sub> adsorption-desorption, X-ray diffraction (XRD), H<sub>2</sub> temperature programmed reduction (H<sub>2</sub>-TPR), CO<sub>2</sub> temperature programmed desorption (CO<sub>2</sub>-TPD), X-ray photoelectron spectroscopy (XPS), transmission electron microscopy (TEM) and scanning electron microscopy (SEM). Temperature profiles along the structured catalytic bed were discussed to interpret the experimental results.

Catalytic performance increased by increasing the Ni content due to enhanced metal-to-support interaction, basicity and oxygen vacancies. Uniform, thin and high-resistance catalytic layers were *in situ* deposited on the cordierite monoliths by the fully reproducible SCS method. Structured catalysts showed high methane productivity per unit weight of catalyst due to simultaneous low catalytic loading and high flow rate. Excellent stability was observed over 200 h of time-on-stream. The results reported in this manuscript pinpointed on the important aspects of realizing CO<sub>2</sub> methanation on structured catalysts, providing a platform for further optimization studies.

### 1. Introduction

A successful transition towards a cleaner and more sustainable energy system in 2050 requires large-scale implementation of sustainable and renewable energy source. In contrast with conventional energy sources, the intermittency and fluctuation of renewable energy make difficult its integration into the existing energy grid [1,2]. Recently, Power-to-Gas (P2G) technologies have been introduced with the aim to store the excess of non-programmable renewable energy. In particular, P2G technologies involve two stage: (i) conversion of electrical power to hydrogen via electrolysis and (ii) conversion of hydrogen to high-value chemicals or fuels thought reaction with CO<sub>2</sub> [3–5]. In this contest, the production of Substitute Natural Gas (SNG) by CO<sub>2</sub> methanation, also called Sabatier reaction, proceeds according to [6,7]:



It is a reaction of great technological and environmental potential, leading to (i) storage of excess H<sub>2</sub> generated from renewable energy, (ii) reduction of CO<sub>2</sub> emissions (greenhouse gas) from the atmosphere and (iii) production of SNG whose distribution infrastructures are readily available [8–10].

CO<sub>2</sub> methanation is a complex reaction because it is strongly exothermic and thermodynamically favored at low temperatures where kinetic rates are low [11]. Moreover, the high concentration of CO<sub>2</sub> involved results in large potential temperature increases and hot spot formation, lowering the yield and leading to catalyst deactivation by sintering and carbon deposition. For these reasons, the catalyst should be active and stable both at low and high temperature [12]. In the last three decades, several systems have been widely investigated as catalyst

\* Corresponding author.

E-mail address: [antonio.vita@itae.cnr.it](mailto:antonio.vita@itae.cnr.it) (A. Vita).

for CO<sub>2</sub> methanation. Between various transition metals (Rh, Ru, Pd, Pt, Fe, Co), Ni-based catalysts seem to be a good choice due to relatively high intrinsic activity and low price [13–15]. Several supports, including Al<sub>2</sub>O<sub>3</sub>, ZrO<sub>2</sub>, SiO<sub>2</sub>, TiO<sub>2</sub>, CeO<sub>2</sub>, MgO and zeolites, were utilized for supported Ni catalysts [16–22]. Moreover, the catalytic performance of Ni catalysts depends on several factors, such as morphology, size and dispersion, oxygen vacancies, ionic conductivity, metal-support interactions, thermal and mechanical stability [23]. These properties depend in turn on the Ni content, the type of support and promoters and the synthesis method [10,24]. Le and co-workers [16] compared the catalytic performance for CO<sub>2</sub> methanation over Ni/CeO<sub>2</sub> catalysts with different Ni contents, whose activity increased by increasing the nickel load, reaching the maximum with the Ni<sub>0.8</sub>Ce<sub>0.2</sub>O<sub>x</sub> system. Tada et al. [25], studied CO<sub>2</sub> methanation performances over Ni-supported catalysts evaluating the effect of electronic interactions between metal phase and support. The participation of CeO<sub>2</sub> effectively promoted the activation of CO<sub>2</sub>, improving the CO<sub>2</sub> methanation performances [25]. Moreover, the addition of Gd<sub>2</sub>O<sub>3</sub> as promoter can modify structural properties, mainly crystallite size and surface area, while simultaneously improving thermal and mechanical resistance of the system [26,27].

The methanation reaction is predominantly carried out in fixed-bed reactors [28]. A structured reactor would be a candidate reaction system providing many advantages such as high surface-to-volume ratio, low pressure drop, good interphase mass transfer and intensification of mass and heat transfer [29–31]. In particular, the fast heat removal from the reactor system allows (i) avoiding limitations in methane yield due to approaching the chemical equilibrium which is a disfavored with increasing temperature and (ii) minimizing catalyst deactivation (metal sintering and carbon deposition) due to thermal stress [32,33]. Fukuhara et al. [32] prepared honeycomb-type Ni/CeO<sub>2</sub> catalysts with high and steady catalytic performance, mainly due to enhanced heat and mass transfer properties [32]. Similar results were reported by Danaci and co-workers [8], studying the CO<sub>2</sub> methanation over macro-porous metal structures coated with Ni/Al<sub>2</sub>O<sub>3</sub> catalyst. Despite the benefits of structured systems, the distribution of the catalytic phase on the surface of the monolithic support is a key factor for the overall system performance. Thus, the coated layer needs to be resistant to thermal and mechanical stresses occurring during methanation reaction [34–36]. As previously reported, the solution combustion synthesis (SCS) method is a suitable procedure to deposit uniform, thin and high-strength catalytic layers on the ceramic monoliths [37–41].

In this work, the catalytic properties of Ni/GDC (gadolinium-doped-ceria) systems in CO<sub>2</sub> hydrogenation were studied. Powder catalysts with different Ni content (15–50 wt.%) were synthesized by the solution combustion synthesis (SCS). Analogously, structured catalysts were prepared by the same method, *in situ* depositing the Ni/GDC (50 wt.% Ni) coating layer on the cordierite monolith (500 cpsi). The catalysts were characterized by N<sub>2</sub> adsorption-desorption, X-ray diffraction (XRD), H<sub>2</sub> temperature programmed reduction (H<sub>2</sub>-TPR), CO<sub>2</sub> temperature programmed desorption (CO<sub>2</sub>-TPD), X-ray photoelectron spectroscopy (XPS), transmission electron microscopy (TEM) and scanning electron microscopy (SEM). CO<sub>2</sub> methanation (H<sub>2</sub>/CO<sub>2</sub> = 4) activity tests were carried out at atmospheric pressure varying temperature (T<sub>SET</sub> = 300–600 °C) and space velocity (GHSV = 10,000–50,000 h<sup>-1</sup>). Stability tests over 200 h of time-on-stream were also performed.

## 2. Experimental

### 2.1. Catalysts preparation

#### 2.1.1. Powder catalysts

Ni/GDC catalysts and GDC support (Ce:Gd molar ratio of 0.8:0.2) were synthesized by the solution combustion synthesis (SCS) method,

previously described [42,43]. The Ni loading was set to 15, 30 and 50 wt.% and confirmed by chemical analysis (ICP/OES). The corresponding catalysts were denoted as 15Ni/GDC, 30Ni/GDC and 50Ni/GDC. High-purity reagent-grade were used as received: nickel nitrate (Ni(NO<sub>3</sub>)<sub>2</sub>·6H<sub>2</sub>O, Aldrich), cerium nitrate (Ce(NO<sub>3</sub>)<sub>3</sub>, Aldrich) and gadolinium nitrate (Gd(NO<sub>3</sub>)<sub>3</sub>·6H<sub>2</sub>O, Aldrich) as metal precursors, while urea (CH<sub>4</sub>N<sub>2</sub>O, Alfa Aesar) as fuel. In a typical experiment, stoichiometric amounts of metal precursors and urea were dissolved in the minimum quantity of distilled water. The amount of fuel was determined according to stoichiometric balance of oxidizing (O) and reducing (F) valences of the components to have an equivalence ratio (O/F) equal to 1 [44]. The obtained solution was introduced into a furnace preheated at 350 °C where the combustion reaction takes place with rapid increase in temperature and gas evolution (N<sub>2</sub>, CO<sub>2</sub>, H<sub>2</sub>O). The resulting powders were calcined at 600 °C in static air for 2 h.

The catalyst (with the sizes of 200–300 μm) was diluted with quartz (with the same sizes) in the 1:1 volume ratio with a total volume of 1.18 cm<sup>3</sup> (diameter 1 cm, length 1.5 cm). The total loading, calculated as quantity of catalytic material per unit volume of catalytic bed, was 0.8 g/cm<sup>3</sup>.

#### 2.1.2. Structured catalysts

Conventional 500 cpsi cordierite monoliths (cylinder form, diameter 1 cm, length 1.5 cm, specific geometric surface 25.2 cm<sup>2</sup>/cm<sup>3</sup>, channels density 77.1 ch/cm<sup>2</sup>, channel size 0.8 mm, wall thickness 320 μm,) were used as support for catalytic layer deposition. Supports were washed in water/acetone (50/50 vol.%) ultrasonic bath for 30 min and dried at 120 °C for 2 h. The catalytic layer (50 wt.% Ni/GDC) was *in situ* deposited by SCS [39,40] dipping each monolith in an aqueous solution containing metal precursors and fuel (as described for powder preparation). The wet monoliths were introduced into a muffle furnace preheated at 600 °C for ca. 10 min, where the combustion reaction occurs, and rapidly cooled down to room temperature in few min. The deposition step was repeated several times to reach the total loading of 0.2 g/cm<sup>3</sup> (denoted as MO-A) and 0.5 g/cm<sup>3</sup> (denoted as MO-B). These quantities corresponded to approximately 25 and 60% of the catalyst employed in the packed bed system. The resulting monoliths were calcined at 600 °C in static air for 2 h. Fig. 1 shows the photographs of the uncoated monolith (a) and the coated MO-B monolith (b).

### 2.2. Catalysts characterization

Specific surface area was estimated according to the Brunauer-Emmet-Teller (BET) equation from adsorption/desorption isotherms at liquid nitrogen temperature (-196 °C) on Micromeritics ASAP 2020 instrument. Prior to measurements the samples were degassed under high vacuum for 6 h at 300 °C.

X-ray diffraction (XRD) experiments were carried out on a Philips X-Pert 3710 diffractometer equipped with a Cu Kα radiation at 40 kV and 20 mA. The patterns were recorded at a scanning speed of 1.50°·min<sup>-1</sup> over the range 2θ = 20°–75°. The peaks were assigned according to the PCPDFWIN database. The CeO<sub>2</sub> and NiO crystallite sizes were calculated using the Scherrer equation based on the main CeO<sub>2</sub> (111) and NiO (200) reflection peaks.

H<sub>2</sub> temperature programmed reduction (H<sub>2</sub>-TPR) was carried out in a Micromeritics ChemiSorb 2750 instrument equipped with a thermal conductivity detector (TCD). A continuous flow of 5% H<sub>2</sub>/Ar (30 NmL/min) was passed over the catalyst in the temperature range 20–1000 °C at a heating rate of 20 °C/min. Before measurements, all samples were heat treated at 500 °C for 1 h under O<sub>2</sub> flow (30 NmL/min). The hydrogen consumption was determined based on the H<sub>2</sub>-TPR patterns of known amounts of CuO.

CO<sub>2</sub> temperature programmed desorption (CO<sub>2</sub>-TPD) was carried out on the same apparatus. The sample was heated up to 800 °C under He flow (30 NmL/min), reduced under H<sub>2</sub> flow (30 NmL/min) at 800 °C for 1 h, cooled to room temperature under He flow (30 NmL/min) and

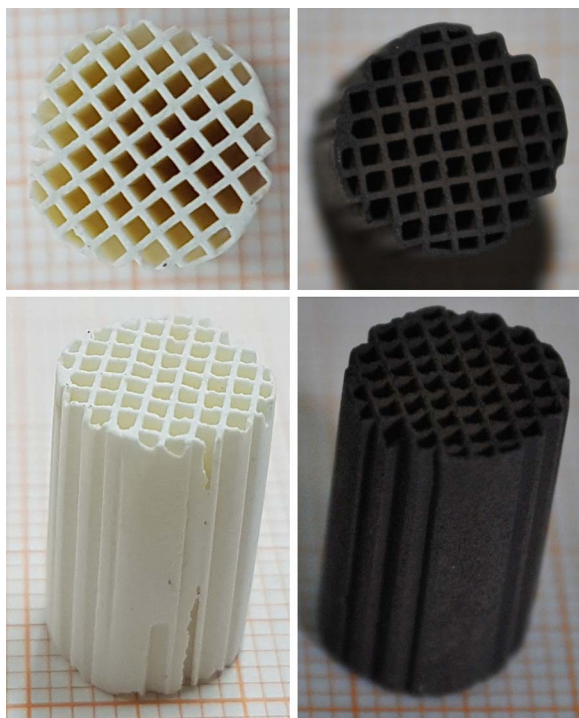


Fig. 1. Photographs of uncoated (left) and coated (right) monoliths.

exposed to CO<sub>2</sub> stream (30 NmL/min) at room temperature for 30 min. The physisorbed CO<sub>2</sub> was removed by He purging at room temperature for 1 h. Then, the temperature was increased with heating rate of 10 °C/min under He flow (30 NmL/min) from 20 to 1000 °C and the desorbed CO<sub>2</sub> was monitored by TCD, which was calibrated by injections of pure CO<sub>2</sub> pulses.

X-ray photoelectron microscopy (XPS) data were collected on a *Physical Electronics GMBH PHI 5800-01* spectrometer operating with a monochromatized Al-K<sub>α</sub> radiation with a power beam of 300 W. The BE regions of C 1 s (275–300 eV), O 1 s (520–540 eV) and Ce 3d (875–925 eV) were investigated, taking the C 1 s line (284.80 eV) of adventitious carbon as reference. The characterisation experiments were carried out for fresh (after reduction) samples.

Transmission electron microscopy (TEM) micrographs were obtained using a *Philips CM12* instrument. The reduced powder samples were dispersed in isopropyl alcohol by ultrasonic treatment and placed on holey copper grids.

The coating procedure was evaluated in terms of homogeneity of the coating, amount of catalyst deposited and adhesion force. Scanning electron microscopy (SEM) images were obtained using a *FEI XL 30* equipped with field emission gun. The structured samples were cut longitudinally to evaluate the thickness of the catalytic layer. The adherence of the coating was evaluated in terms of weight loss after two ultrasonic treatment in 50 vol.% isopropyl alcohol solution. The monoliths were treated for 30 min at 45 kHz and 130 W using the *USC 900D* ultrasonic bath.

### 2.3. Methanation performance

CO<sub>2</sub> methanation was carried out in a quartz tubular fixed-bed reactor (1 cm inner diameter, 25 cm length) horizontally placed in a furnace under atmospheric pressure. Both powder and structured catalysts were placed in the centre of the quartz tube. The catalyst was heated to 800 °C (15 °C/min) under N<sub>2</sub> flow (30 NmL/min), reduced at 800 °C for 1 h under 50 vol.% H<sub>2</sub>/N<sub>2</sub> stream (30 NmL/min) and cooled down to reaction temperature (T<sub>SET</sub>) under N<sub>2</sub> flow (30 NmL/min) before starting the catalytic test. Four chromel/alumel thermocouples

were employed at a distance of 0.1 (T<sub>SET</sub>), 0.2 (T<sub>IN</sub>), 0.5 (T<sub>CENT</sub>) and 1.4 cm (T<sub>OUT</sub>) from the beginning of the catalytic bed (length 1.5 cm). The first thermocouple, connected with a PID controller, was used to regulate the reaction temperature (T<sub>SET</sub>), while the others were used to measure the temperature profile along the catalytic bed. A mixture gas of H<sub>2</sub>/CO<sub>2</sub>/N<sub>2</sub> with fixed molar ratio 4/1/1 was fed into the reactor by mass flow-controliers (*Brooks Instrument Smart Mass Flow*). An *Agilent 6890 Plus* gaschromatograph, equipped with thermal conductivity (TCD) and flame ionization (FID) detectors, was used to on-line analyze reactants and products every 20 min N<sub>2</sub> was used as internal standard for mass balance calibration.

Activity tests (8 h each) were carried out varying temperature (T<sub>SET</sub> = 300–600 °C) and space velocity (GHSV = 10,000–50,000 h<sup>-1</sup>). Stability tests over 200 h of time-on-stream were also performed at T<sub>SET</sub> = 400 °C and GHSV = 30,000 h<sup>-1</sup>. The experimental results were reported as CO<sub>2</sub> conversion and molar concentrations of H<sub>2</sub>, CO, CO<sub>2</sub> and CH<sub>4</sub>. Thermodynamic analysis, performed by the simulation package *HSC Chemistry*<sup>®</sup> 7, involved the determination of equilibrium compositions of the system at specified operating conditions (temperature, pressure). The model was based on the minimization of Gibbs free-energy of the existing species (CH<sub>4</sub>, H<sub>2</sub>O, CO<sub>2</sub>, CO, H<sub>2</sub>, solid carbon). This method does not require any detail of chemical reactions taking place in the system while it is based on the concept that at chemical equilibrium the total Gibbs energy of the system has its minimum value [45].

## 3. Results and discussion

### 3.1. Powder and structured catalysts characterization

The main textural properties of the synthesized GDC support and Ni/GDC catalysts are reported in Table 1. The surface area ranged from 19.5 to 33.8 m<sup>2</sup>/g. It could be observed that the incorporation of nickel led to surface area (24.5 for 15Ni/GDC) higher than the GDC support (19.5 m<sup>2</sup>/g). Moreover, the surface area slightly increased to 33.8 m<sup>2</sup>/g by increasing the Ni content to 50 wt.% (50Ni/GDC). The diffraction patterns of the calcined samples are displayed in Fig. 2. All the systems showed the XRD peaks for the face-centered cubic phase of CeO<sub>2</sub> (JCPDS Card 4–593), while the absence of the Gd<sub>2</sub>O<sub>3</sub> crystallographic planes suggested the amorphous nature of Gd<sub>2</sub>O<sub>3</sub> or its presence as Ce<sub>0.8</sub>Gd<sub>0.2</sub>O<sub>x</sub> solid solution. The CeO<sub>2</sub> average crystallite size calculated from the Scherrer equation, based on the main CeO<sub>2</sub> (111) reflection peak, decreased by increasing the Ni loading (Table 1). As previously reported, the textural features of synthesized powders strongly depend on the flame temperature achieved during the combustion reaction [42]. The theoretical adiabatic flame temperature (T<sub>ad</sub>) was calculated using the thermodynamic data for reactants and products by the equation:

$$T_{ad} = T_0 \frac{\Delta H_r - \Delta H_p}{C_p} \quad (1)$$

Table 1  
Nickel loading, surface area and crystallite size of the synthesized powders.

Sample	Ni content <sup>a</sup> (wt. %)	S <sub>BET</sub> (m <sup>2</sup> /g)	XRD		
			CeO <sub>2</sub> Lattice parameter <sup>b</sup> (nm)	CeO <sub>2</sub> Particle size <sup>c</sup> (nm)	NiO Particle size <sup>c</sup> (nm)
GDC	–	19.5	0.5387	11.3	–
15Ni/GDC	15.1	24.5	0.5378	8.0	6.0
30Ni/GDC	30.4	27.0	0.5378	7.8	7.5
50Ni/GDC	49.8	33.8	0.5377	7.7	9.2

<sup>a</sup> Determined by ICP/OES chemical analysis.

<sup>b</sup> Calculated by the relation  $\alpha = \sqrt{h^2 \cdot k^2 \cdot l^2} \cdot (\lambda / 2 \cdot \sin \theta)$ .

<sup>c</sup> Calculated by the Sherrer equation of the CeO<sub>2</sub> (111) and NiO (200) reflections.

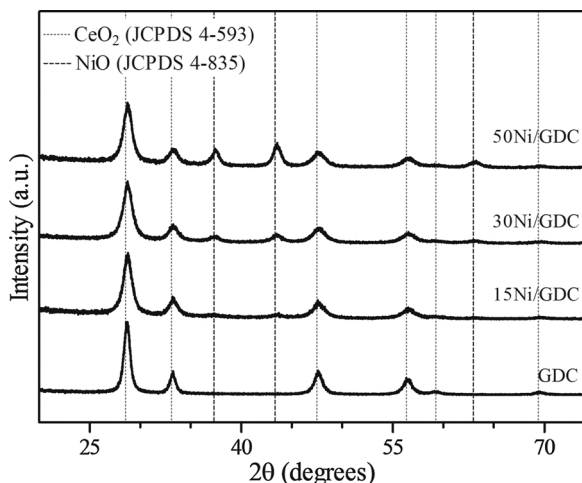


Fig. 2. XRD patterns of the synthesized GDC support and Ni/GDC catalysts.

where  $\Delta H_r$  and  $\Delta H_p$  are the formation enthalpies of reactants and products, respectively,  $C_p$  is the molar heat capacity of products at constant pressure and  $T_0$  is the ignition temperature. The derived flame temperatures of the prepared samples followed the order: 50Ni/GDC ( $1250^\circ\text{C}$ ) < 30Ni/GDC ( $1288^\circ\text{C}$ ) < 15Ni/GDC ( $1310^\circ\text{C}$ ) < GDC ( $1318^\circ\text{C}$ ). Indeed, flame temperature decreased by increasing the Ni content, leading to higher surface area and lower  $\text{CeO}_2$  particle size values (Table 1). Peaks of  $\text{NiO}$  (JCPDS 4–835) could be observed in all Ni/GDC catalysts, the intensity of which increased by increasing the Ni content, due to the formation of larger  $\text{NiO}$  particles. Indeed, the  $\text{NiO}$  crystallite size slightly increased from 6.0 (15Ni/GDC) to 9.2 (50Ni/GDC). Moreover, the lattice parameter decreased with introducing the Ni metal phase (Table 1). The pure GDC support had a lattice parameter of 0.5387 nm, while the Ni-based systems showed lattice parameters of 0.5377–0.5378 nm, indicating the partial substitution of  $\text{Ce}^{4+}$  (0.097 nm) with smaller  $\text{Ni}^{2+}$  (0.081 nm) ions and resulting in the shrinkage of the  $\text{CeO}_2$  cell due to the formation of Ce-Gd-Ni-O solid solution.

The reducibility of the combustion-synthesized samples was studied by  $\text{H}_2$ -TPR and the results are displayed in Fig. 3. The reduction of bare GDC support showed two main reduction peaks at 550 and  $860^\circ\text{C}$  due to the reduction of  $\text{CeO}_2$  surface oxygen and  $\text{CeO}_2$  bulk oxygen, respectively [26,46]. The TPR profiles of Ni-based systems showed two main reduction peaks centered at 380 and  $450^\circ\text{C}$ , attributed to the reduction of bulk  $\text{NiO}$  species with different extent interactions with the

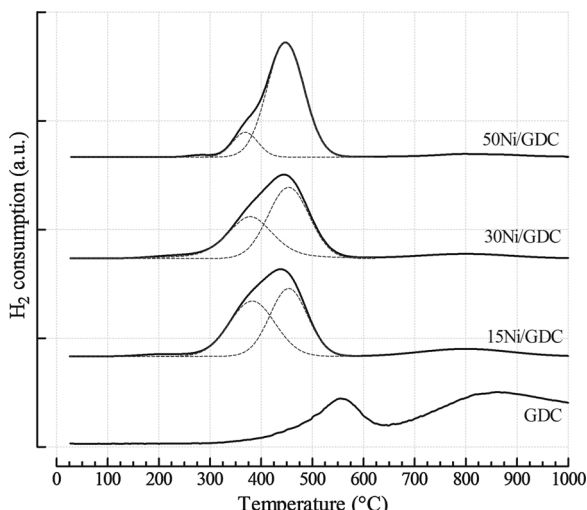


Fig. 3. TPR profiles of synthesized GDC support and Ni/GDC catalysts.

support [14,47,48]. Generally, the reduction of bulk  $\text{NiO}$  (not reported) occurs in the temperature range of  $280$ – $300^\circ\text{C}$  [49]. The shift to higher temperature of this reduction peak suggested the presence of strong Ni-support interactions [10,49,50]. Moreover, as the Ni loading increased, the high temperature reduction peak became greater in intensity, due to the more pronounced metal-support interaction and to the contribution of larger  $\text{NiO}$  crystallites, in accordance with XRD evidences (Fig. 2) [51]. Table 2 shows the experimental/theoretical hydrogen consumption and the relative reducibility of the synthesized samples. The experimental  $\text{H}_2$  consumption, expressed as mmol $_{\text{H}_2}$  per gram of catalyst, was related to the TPR peaks up to  $600^\circ\text{C}$ . In addition, theoretical amount of  $\text{H}_2$  demanded was calculated by assuming complete reduction of  $\text{NiO}$  to  $\text{Ni}$  for Ni/GDC samples (Table 2). The reducibility of the catalysts decreased with increasing the Ni loading from 91.5% (15Ni/GDC) to 88.4 (30Ni/GDC) and 87.1% (50Ni/GDC). This could be due to the presence of Ce-Gd-Ni-O solid solution, more difficult to reduce, and to the formation of larger  $\text{NiO}$  particles, as confirmed by XRD analysis. Similar results were reported by Singha et al. [52], indicating that the core of larger  $\text{Ni}$  oxide particles was not readily exposed to hydrogen for reduction.

Fig. 4 shows the  $\text{CO}_2$ -TPD of the Ni/GDC catalysts with various Ni amounts, while the quantitative analysis of the desorbed  $\text{CO}_2$  is reported in Table 3. All the catalysts exhibited three main desorption peaks, due to adsorption sites with increasing strength: (a) weak  $\text{CO}_2$  adsorption sites situated at low temperatures ( $T < 250^\circ\text{C}$ ); (b) moderate  $\text{CO}_2$  adsorption sites at temperature ranging between 250 and  $750^\circ\text{C}$ ; (c) strong  $\text{CO}_2$  adsorption sites situated at high temperature ( $T > 700^\circ\text{C}$ ) [53]. The desorption profiles in Fig. 4 revealed that the major contribution is due to the presence of moderate-basic sites, following the order 15Ni/GDC ( $43.8 \mu\text{mol}_{\text{CO}_2}/\text{g}$ ) < 30Ni/GDC ( $59.7 \mu\text{mol}_{\text{CO}_2}/\text{g}$ ) < 50Ni/GDC ( $75.2 \mu\text{mol}_{\text{CO}_2}/\text{g}$ ). The same order was observed for the basic site density, expressed as  $\text{CO}_2$  adsorbed per unit volume of catalytic bed (Table 3). Besides, weak-basic sites concentration seemed to be not affected by the nickel content, while the amount of medium- and strong-basic sites increased by increasing the Ni loading (Table 3). Thus, the increase in Ni content led to higher basicity mainly due to the stronger Ni-support interaction, as confirmed by TPR analysis [54,55].

Fig. 5 presents the XPS spectra in the O 1 s and Ce 3d regions for the Ni/GDC samples. A nonlinear least-square fitting procedure using Gaussian and Lorentzian type curves showed O 1 s spectra with two distinct peaks [56,57]. The intense peak at  $528.9 \text{ eV}$  could be attributed to the surface lattice oxygen ( $\text{O}_\alpha$ ) of GDC, while the signal at  $531.7 \text{ eV}$  could be assigned to the surface hydroxyl groups or the adsorbed oxygen ( $\text{O}_\beta$ ) [58,59]. Based on the area integrals of the oxygen species, the ratio of  $\text{O}_\alpha$  to  $\text{O}_T$  ( $\text{O}_T = \text{O}_\alpha + \text{O}_\beta$ ) for all catalysts was estimated and summarized in Table 4. It can be seen that the percentage of surface lattice oxygen ( $\text{O}_\alpha$ ) decreased by increasing the Ni content. In particular, the  $\text{O}_\alpha/\text{O}_T$  ratio decreased from 84.5 to 79.7% for 15Ni/GDC and 30Ni/GDC catalysts, respectively, while a slight decrease to 79.1% was observed further increasing the Ni content (50Ni/GDC). Such behavior could be ascribed to the increasing number of oxygen vacancies caused by the insertion of the  $\text{Ni}^{2+}$  cations on the GDC support, in accordance with XRD evidences [60,61].

The interpretation of the Ce 3d photoemission spectra is not straightforward mainly due to multielectric processes both in the  $\text{Ce}^{4+}$  and  $\text{Ce}^{3+}$  states [56]. The XPS spectra in Fig. 5 could be deconvoluted into ten peaks, corresponding to four pairs of spin-orbit doublets [23,62]. Generally, the peaks marked as v, v'', v''', u, u'' and u''' arise from the contribution of  $\text{Ce}^{4+}$  species, while the peaks labeled as v°, v'', u°, and u''' originate from the contribution of  $\text{Ce}^{3+}$  species [62,63]. According to the ratio of  $\text{Ce}^{3+}$  ion peaks area to that of the total  $\text{Ce}^{3+}$  and  $\text{Ce}^{4+}$  ion peaks area, the following equation was used to calculate the relative content of  $\text{Ce}^{3+}$ :

**Table 2**

Experimental/theoretical hydrogen consumption and relative reducibility from TPR profiles of the Ni/GDC catalysts.

Sample	Experimental H <sub>2</sub> consumption (mmol <sub>H2</sub> /g)			Theoretical H <sub>2</sub> consumption (mmol <sub>H2</sub> /g)	Reducibility (%)
	Low temperature peak	High temperature peak	Total		
15Ni/GDC	1.14	1.17	2.31	2.53	91.5
30Ni/GDC	1.78	2.72	4.50	5.09	88.4
50Ni/GDC	0.95	6.31	7.26	8.34	87.1

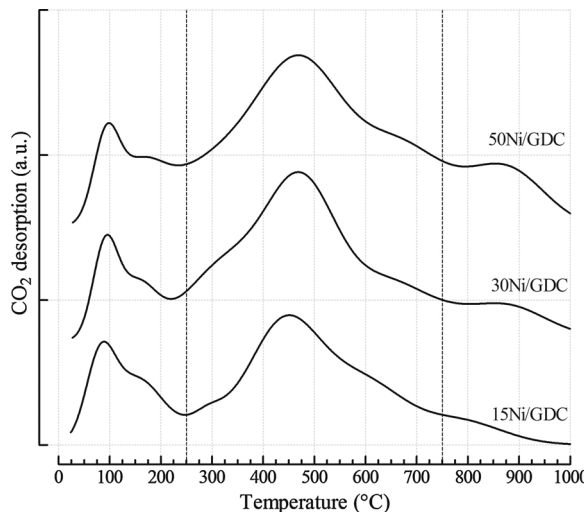
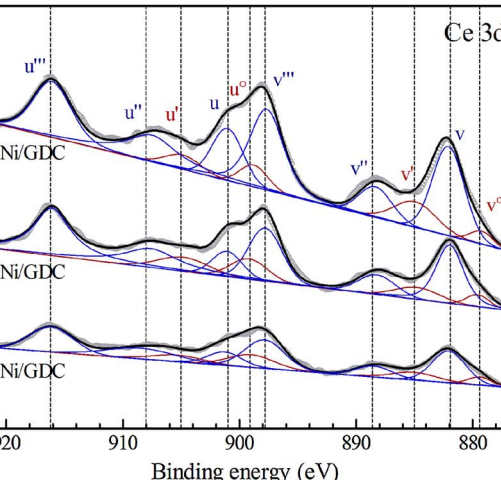
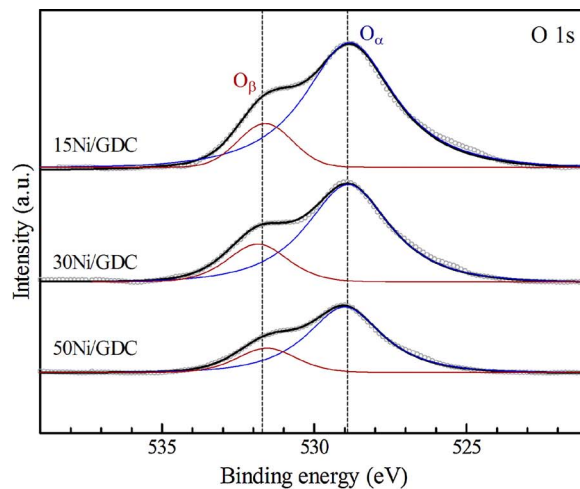
Fig. 4. CO<sub>2</sub>-TPD of 15Ni/GDC, 30Ni/GDC and 50Ni/GDC catalysts.

Fig. 5. High resolution XPS spectra of the Ni/GDC catalysts.

**Table 3**CO<sub>2</sub>-TPD analysis for determining basic properties of the Ni/GDC catalysts.

Sample	CO <sub>2</sub> desorption (μmol <sub>CO2</sub> /g)			Basic site density <sup>a</sup> (μmol <sub>CO2</sub> /cm <sup>3</sup> )
	Weak (< 250 °C)	Moderate (250–750 °C)	Strong (> 750 °C)	
15Ni/GDC	17.1	43.8	4.0	64.9
30Ni/GDC	16.9	59.7	10.1	86.7
50Ni/GDC	17.5	75.2	18.2	110.9
				60.2

<sup>a</sup> Expressed as moderate (250–750 °C) basic sites per unit volume of catalytic bed.

$$\text{Ce}^{3+} = \frac{u'' + u' + v'' + v'}{\sum (u + v)} \quad (2)$$

The corresponding calculation results are summarized in Table 4. The relative content of Ce<sup>3+</sup> increased by increasing the Ni content, due to the formation of more oxygen vacancies in the ceria lattice. Besides, the 50Ni/GDC catalyst showed the highest Ce<sup>3+</sup> surface content (21.8%), indicating a more pronounced metal-support interaction, which is consistent with the above TPR results [62,63].

The morphology of 50Ni/GDC catalyst was checked by TEM analysis. TEM images in Fig. 6a showed 30–50 nm CeO<sub>2</sub> particles in agglomerate form. Not very uniform sized Ni particles, ranging between 10 and 25 nm, were revealed. More in detail, Images 5b and 5c show the magnifications of two areas of Fig. 6a; fringes with d-spacing 2.0 Å were attributed to the (111) planes of Ni, whereas fringes with 3.1 Å were attributed to the (111) planes of CeO<sub>2</sub> crystals.

Figs. 7 and 8 show SEM images of bare and coated monoliths. A reduction of the macro-porosity of the bare cordierite (Fig. 7a) was revealed after the in-situ deposition of the catalytic layer (Fig. 7b). Well uniform coating layers were found, as evidenced in the corner (Fig. 7b), inner (Fig. 7c,d) and frontal (Fig. 7e) channel views and from the EDX mapping (Fig. 7f) of the coated MO-B monolith. Moreover, the magnification of the coated layer (Fig. 7d) confirmed the presence of a

**Table 4**

Summary of XPS data for the Ni/GDC catalysts.

Sample	Relative content of O <sub>α</sub> (%) <sup>a</sup>	Relative content of Ce <sup>3+</sup> (%) <sup>b</sup>
15Ni/GDC	84.5	16.3
30Ni/GDC	79.7	20.1
50Ni/GDC	79.1	21.8

<sup>a</sup> Calculated according to the ratio O<sub>α</sub>/O<sub>T</sub>, based on the area integrals in the O 1s spectra (O<sub>T</sub> = O<sub>α</sub> + O<sub>β</sub>).<sup>b</sup> Calculated according to Eq. (2), based on the area integrals in the Ce 3d spectra.

significant residual porosity due to the escaped gas during the SCS steps, as previously reported [40–42]. Average thickness of ca. 10 μm for low-loaded system (MO-A, Fig. 8a) and 40 μm for high-loaded system (MO-B, Fig. 8b) were determined.

The mechanical resistance of the coated layers, evaluated by ultrasonic treatment in isopropyl alcohol solution, evidenced good adherence of the catalytic layer to the cordierite support. Negligible

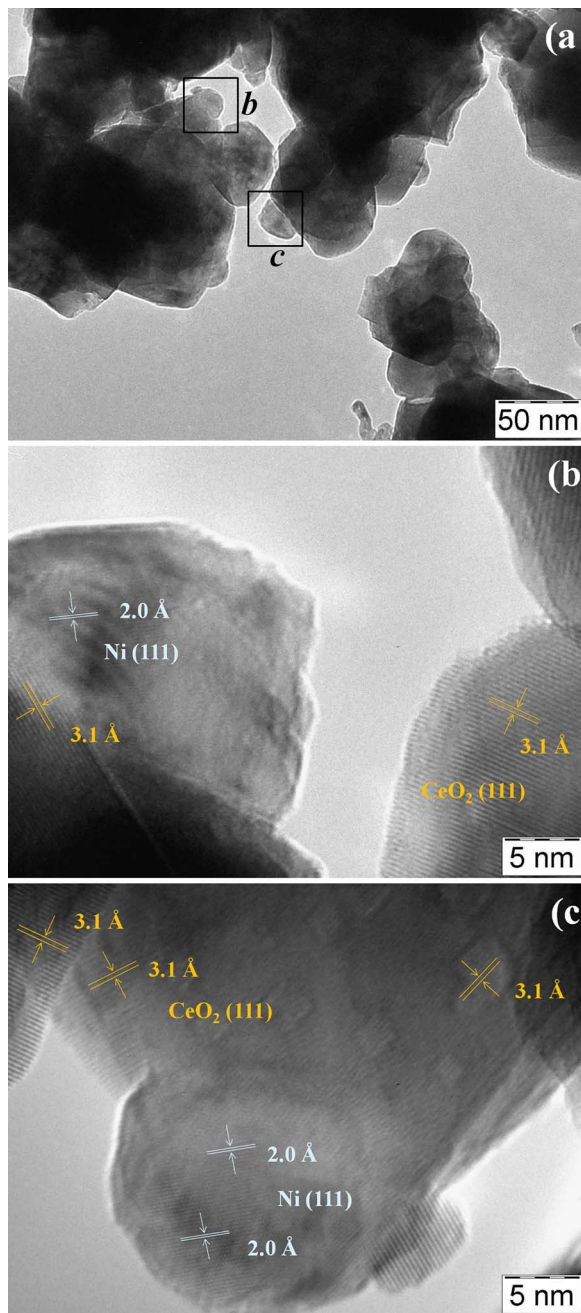


Fig. 6. TEM micrographs of the 50Ni/GDC catalyst.

weight loss of ca. 0.3–0.5% after the second adhesion test (calculated on the total weight of the monolith) were found.

### 3.2. Catalytic activity

#### 3.2.1. Powder catalyst: effect of Ni content and reaction temperature

Fig. 9 shows the products distribution of CO<sub>2</sub> methanation at equilibrium calculated via the Gibbs free energy minimization method at 1 atm for a feed gas containing H<sub>2</sub> and CO<sub>2</sub> with a stoichiometric H<sub>2</sub>/CO<sub>2</sub> molar ratio of 4. At relatively low temperature (200–300 °C), CH<sub>4</sub> and H<sub>2</sub>O were the main reaction products. Increasing the temperature, the methanation reaction was disfavoured due to its exothermic nature, leading to increased amounts of unreacted CO<sub>2</sub> and H<sub>2</sub>, along with decreased amounts of produced CH<sub>4</sub>. Moreover, at temperature higher than 450 °C the reverse water gas shift (RWGS) reaction was favoured, resulting in the increase of CO by-product. However, when the

temperature exceeded 550 °C, the mole fraction of CO<sub>2</sub> reached its maximum and then decreased because the RWGS reaction dominated [64].

The mass transfer in a porous catalyst is a significant factor in determining the catalytic activity [65]. As reported by other Authors, the external diffusion limitation is negligible when the rate of the surface reaction is sufficient slow [66,67]. On the other hand, the internal diffusion limitation was estimated by the Weisz-Prater criteria, according to:

$$N_{WP} = \frac{\mathfrak{R} \cdot R_p^2}{C_s \cdot D_{eff}} < 1 \quad (3)$$

where  $\mathfrak{R}$  is the reaction rate of CO<sub>2</sub> per unit volume of the catalyst ( $1.48 \times 10^{-5}$  mol/cm<sup>3</sup> s);

$R_p$  is the particle radius of catalyst ( $1.25 \times 10^{-2}$  cm);

$C_s$  is the surface concentration of CO<sub>2</sub> ( $3.02 \times 10^{-6}$  mol/cm<sup>3</sup>), assumed equal to the bulk CO<sub>2</sub> concentration ad calculated by the equation  $C_s = P_{CO_2}/RT$ ;

$D_{eff}$  is the pore diffusion ( $3.41 \times 10^{-2}$  cm<sup>2</sup>/s), dominated by Knudsen diffusion ( $D_{Kn}$ ) and calculated by  $D_{eff} \approx D_{Kn} = 1/3\nu d$ , where  $\nu$  is the average molecular velocity ( $5.69 \times 10^4$  cm/s) and  $d$  is the average pore diameter ( $1.80 \times 10^{-6}$  cm).

Under the selected reaction conditions (i.e.  $P=1$  atm,  $T=673$  K), the value of  $N_{WP}$  for the 50Ni/GDC catalyst was 0.022, indicating a negligible internal mass transfer limitation [67].

CO<sub>2</sub> conversion (Fig. 10a) and effluent composition (Fig. 10b) measured during the catalytic tests carried out at atmospheric pressure are plotted in Fig. 10, as a function of Ni content (15–50 wt.%) and reaction temperature ( $T_{SET} = 300$ –600 °C). As comparison, the equilibrium values of the CO<sub>2</sub> conversion were also reported as dotted gray line. For all the catalysts, the conversion increased by increasing the temperature, reaching the maximum at ca. 450–500 °C and decreasing afterward (Fig. 10a). As reported by several Authors, low temperatures were thermodynamically beneficial to the reaction but kinetically disadvantage due to the slow reaction rate [4,15,16,32]. Indeed, the 15Ni/GDC showed ca. 35% of CO<sub>2</sub> conversion at 300 °C, that increased to ca. 64% at 450 °C, remaining below the thermodynamic limits; this could be due to the great kinetic barrier for the full reduction of CO<sub>2</sub> (+4) to CH<sub>4</sub> (-4), an eight-electron process which required high activation energy [68]. Further increase in the reaction temperature led to a slightly decrease in the CO<sub>2</sub> conversion to ca. 60% at 600 °C, due to thermodynamic limit of methanation reaction and to the occurrence of RWGS reaction [32,68,69].

The variation on CH<sub>4</sub> concentration in the products mixture followed the same trend, increasing from ca. 9% at 300 °C to 17% at 450 °C and then decreasing to 8% at 600 °C (Fig. 10b). Apparently, this phenomenon was not thermodynamically consistent, because methane concentration should decrease by increasing temperature (Fig. 9) due to methanation equilibrium, suggesting that the methanation on the 15Ni/GDC catalyst at relative low temperatures ( $T_{SET} < 450$  °C) was probably a kinetic controlled reaction [15]. Moreover, the CO byproduct concentration increased from 0.2 to 5.1% by increasing temperature from 400 to 600 °C due to the RWGS equilibrium.

The results showed that the increase in Ni loading positively affected the activity at all the investigated reaction temperature. The synthesized systems followed the methanation activity order: 50Ni/GDC > 30Ni/GDC > 15Ni/GDC. However, it is important to note that only slight variations in the catalytic activity were observed by increasing the Ni content. The 50Ni/GDC sample showed ca. 44% of CO<sub>2</sub> conversion at 300 °C, that reached the highest value of ca. 71% at 450 °C and then decreased to 65% at 600 °C (Fig. 10a). Despite several studies, the mechanism of CO<sub>2</sub> methanation is still under debate. Some authors suggested that CO<sub>2</sub> is first dissociated into CO either directly [70,71] or through carbonate and/or formate intermediates [72,73]. The formed CO would be then dissociated into C and O atoms on the

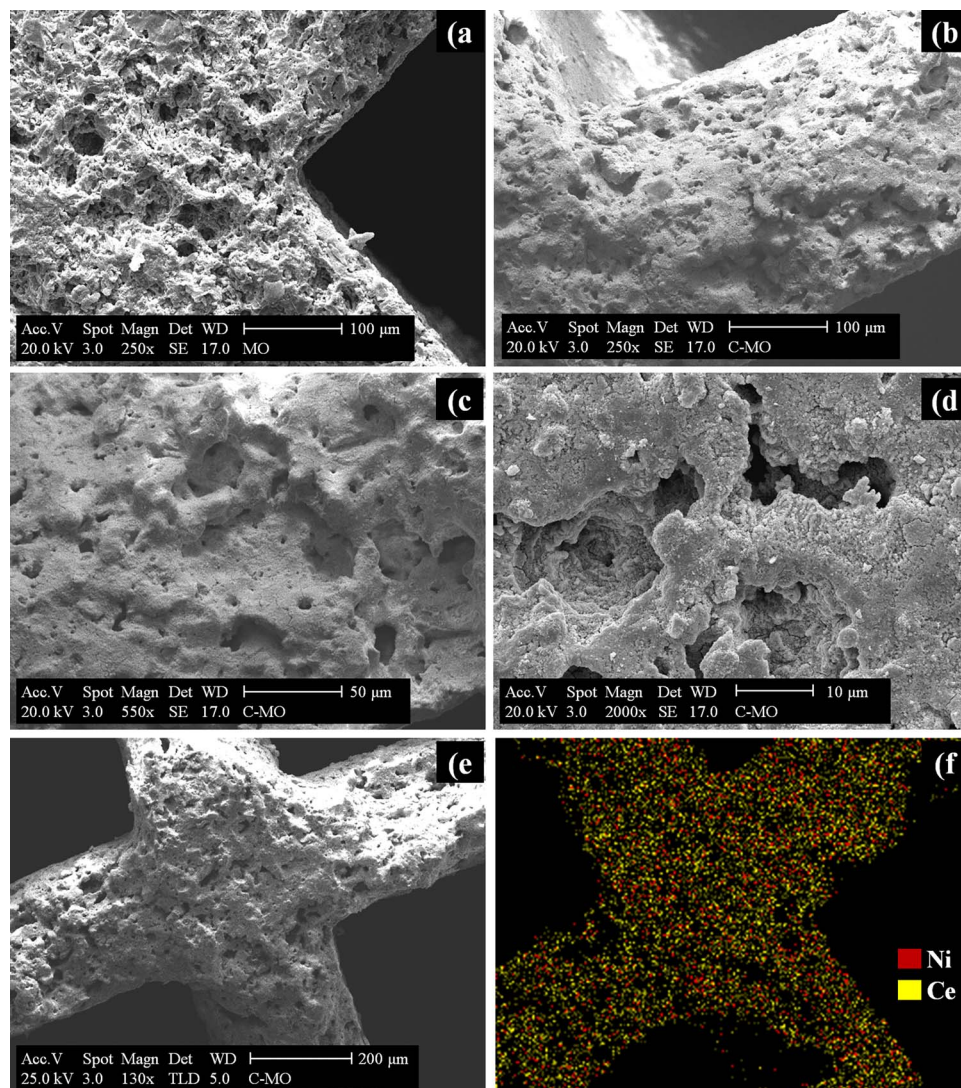


**Fig. 7.** SEM micrographs of the bare and coated (MO-B) monoliths: corner channel view of bare (a) and coated monoliths (b), inner channels view at different magnification of coated monoliths (c,d), frontal channel view (e) and corresponding EDX mapping (f) of coated monolith.

metal sites and further hydrogenated into methane [74]. Instead, other authors assumed that CO<sub>2</sub> methanation does not require CO as reaction intermediate but occurs via carbonates and formates which are directly hydrogenated into CH<sub>4</sub> [75–77]. However, for both mechanisms, the CO<sub>2</sub> adsorption on the basic sites of the catalyst is one of the key points to provide high methanation performance [14,18,32]. Thus, the enhanced activity of the 50Ni/GDC catalyst could be explained by the superior metal-to-support interactions and the increased number of moderate-basic sites, as confirmed by TPR and TPD characterization results. In addition, the presence of Ce<sup>3+</sup>/Ce<sup>4+</sup> ion pairs and the

oxygen vacancies in the GDC support, as shown by the XPS analysis, could contribute to enhance the adsorption and activation of CO<sub>2</sub> [23]. On this basis, the 50%Ni/GDC catalytic formulation was selected to prepare monolith-type structured systems.

### 3.2.2. Structured catalysts: effect of catalyst loading, reaction temperature and space velocity

To estimate the influence of external and internal mass transfer limitation, the Carberry (Ca) and Weisz-Prater (WP) numbers were calculated according to the following equations [78,79]:

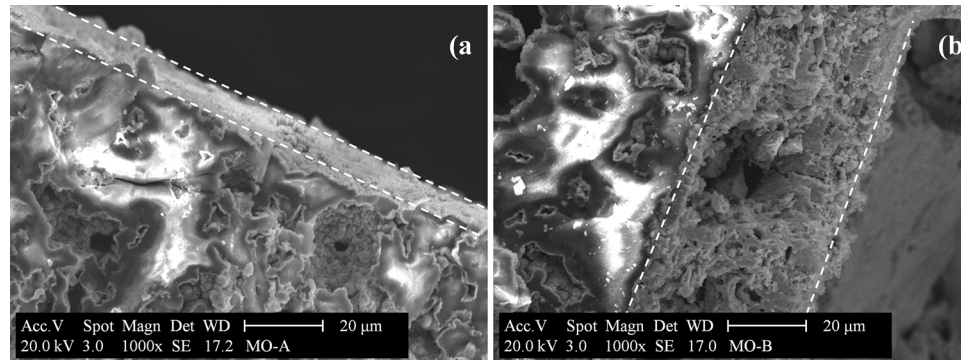


**Fig. 8.** SEM images of MO-A (a) and MO-B (b) coated layers.

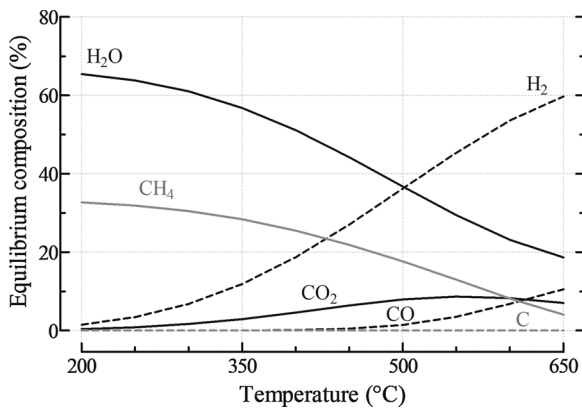


Fig. 9. Thermodynamic equilibrium analysis of CO<sub>2</sub> methanation: effect of temperature on products composition (H<sub>2</sub>/CO<sub>2</sub> = 4/1 molar, P = 1 atm).

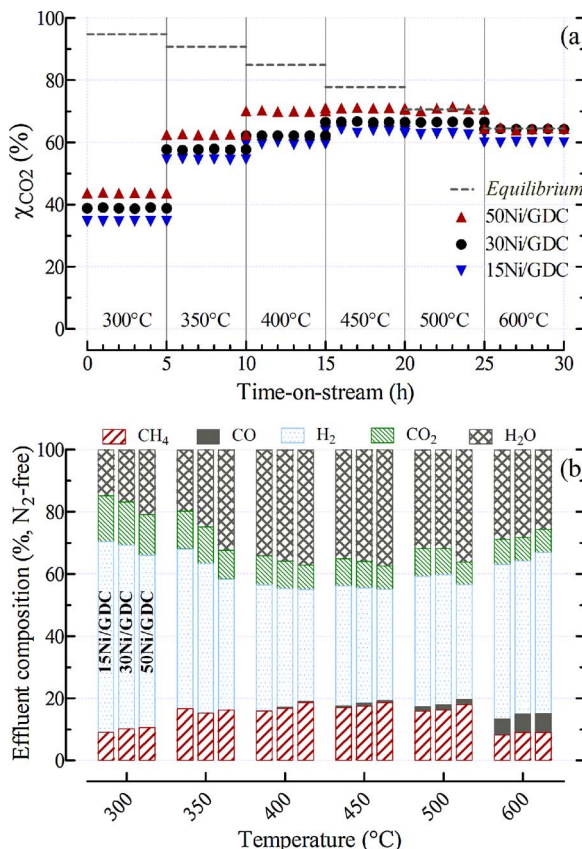


Fig. 10. CO<sub>2</sub> conversion (a) and effluent composition (b) over powder Ni/GDC catalysts. Influence of nickel content (15–50 wt.%) and set temperature (300–600 °C). Reaction conditions: H<sub>2</sub>/CO<sub>2</sub>/N<sub>2</sub>: 4/1/1 molar, GHSV: 10,000 h<sup>-1</sup>, total gas flow: 200 Nml/min, catalyst: 0.8 g/cm<sup>3</sup>.

$$Ca = \frac{r_{CO_2} \cdot \rho_{cat}}{k_G \cdot a_m \cdot C_{CO_2}} < \frac{0.05}{n} \quad (4)$$

$$WP = \frac{r_{CO_2} \cdot \rho_{cat} \cdot \delta_c^2}{D_{CO_2,e} \cdot C_{CO_2}} < \frac{n + 1}{2} < 1 \quad (5)$$

where  $r_{CO_2}$  is the observed reaction rate with respect of CO<sub>2</sub> ( $8.51 \times 10^{-5}$  kmol/kg s);

$\rho_{cat}$  is the density of the catalytic layer ( $1.50 \times 10^3$  kg/m<sup>3</sup>);  $k_G$  is the mass transfer coefficient ( $4.87 \times 10^{-1}$  m/s), calculated by equation  $k_G = S_h D_{CO_2}/d_h$ , where  $S_h$  is the Sherwood number (2.99),  $D_{CO_2}$  is the diffusivity of CO<sub>2</sub> in gas phase ( $1.35 \times 10^{-4}$  m<sup>2</sup>/s) and  $d_h$  is the hydraulic diameter ( $8.24 \times 10^{-4}$  m);

$a_m$  is the specific geometric surface area of monolith ( $2.52 \times 10^3$  m<sup>2</sup>/m<sup>3</sup>);

$C_{CO_2}$  is the CO<sub>2</sub> concentration in gas mixture ( $7.44 \times 10^{-3}$  kmol/m<sup>3</sup>);

$\delta_c$  is the characteristic coating layer dimension ( $4 \times 10^{-5}$  m);

$D_{CO_2,e}$  is the effective diffusivity of CO<sub>2</sub> in the catalyst pores ( $7.73 \times 10^{-7}$  m<sup>2</sup>/s), assuming catalyst porosity and tortuosity equal to 0.57 and 4, respectively [80].

Under the selected reaction conditions (i.e. P = 1 atm, T = 673 K, GHSV = 30,000 h<sup>-1</sup>, MO-B structured catalyst), the calculated Ca and WP numbers for a first-order reaction rate (n = 1) were 0.014 and 0.035, respectively, confirming the absence of external and internal mass transfer limitations [78,79,81].

Fig. 11 shows the CO<sub>2</sub> conversion measured during methanation experiments over the structured catalysts with different catalyst loading (0.2 g/cm<sup>3</sup> in MO-A and 0.5 g/cm<sup>3</sup> in MO-B). Tests were carried out at atmospheric pressure, increasing the reaction temperature (T<sub>SET</sub>) from 300 to 600 °C at GHSV of 10,000 (Fig. 11a), 30,000 (Fig. 11b) and 50,000 h<sup>-1</sup> (Fig. 11c), respectively. The temperature difference ( $\Delta T$ ) between the reaction temperature (T<sub>SET</sub> = 350 °C) and the catalyst-bed temperature (T<sub>IN</sub>, T<sub>CENTR</sub>, T<sub>OUT</sub>) is also depicted in Fig. 11d-f. The effluent compositions and the temperature profiles along the catalytic bed are summarized in Tables 5 and 6 for both MO-A and MO-B structured catalysts, respectively.

Poor activity was observed over the MO-A system at all the investigated GHSV (Fig. 11a-c). At GHSV of 10,000 h<sup>-1</sup>, the CO<sub>2</sub> conversion increased from 7 to 66% by increasing temperature up to 400 °C, remaining lower than the equilibrium values due to kinetic limitations. At 450 °C, the CO<sub>2</sub> conversion (70%) approached the equilibrium value and slightly decreased to 63% by increasing the temperature up to 600 °C; this could be due to the thermodynamic limitation of methanation reaction and to the occurrence of the competitive RWGS reaction (Fig. 11a). Increasing the space velocity up to 30,000 (Fig. 11b) and 50,000 h<sup>-1</sup> (Fig. 11c), the CO<sub>2</sub> conversion decreased mainly due to the insufficient quantity of catalyst (0.2 g/cm<sup>3</sup>) especially at decreased contact time between reactants and catalyst. Analogously, the variation on CH<sub>4</sub> concentration in the products mixture showed the same trend (Table 5). These evidences could be related to the temperature profiles recorded along the catalytic bed (Fig. 11d-f, Table 5). The low-loaded MO-A monolith showed an almost flat temperature profile; as methanation is an exothermic reaction, this highlighted the poor reactivity of the sample. Indeed, the temperature values recorded along the catalytic bed were almost coincident with the set temperature, i.e. 355 (T<sub>IN</sub>), 361 (T<sub>CENTR</sub>) and 359 °C (T<sub>OUT</sub>) at T<sub>SET</sub> = 350 °C and GHSV = 10,000 h<sup>-1</sup> (Table 5). Increasing the GHSV up to 50,000 h<sup>-1</sup>, lower temperatures were recorded along the catalytic bed (Table 5), due to the cooling effect induced by the reagents flow.

At relatively low space velocity, comparable activity was observed for the both structured catalysts (Fig. 11a), while higher activity was revealed for the MO-B system at GHSV of 30,000 and 50,000 h<sup>-1</sup> (Fig. 11b,c). This behavior, mainly due to the increased catalyst loading (0.5 g/cm<sup>3</sup>), is closely related to the temperature profiles recorded along the catalytic bed (Fig. 11d-f, Table 6). Although the high space velocity could create unfavorable conditions for the catalytic activity due to the short contact time, the activity of the MO-B system increased by increasing the GHSV from 10,000 to 50,000 h<sup>-1</sup> (Fig. 11), due to the higher temperatures recorded along the catalytic bed [82,83]. The high activity of the high-loaded MO-B system led to large amounts of released heat, induced by the strong exothermicity of CO<sub>2</sub> methanation, inevitably increasing the temperature along the catalytic bed [84]. Thus, the increasing of space velocity resulted in a much greater  $\Delta T$  (temperature difference between the set reaction temperature and the catalytic bed temperatures) as reported in Fig. 11d-f. For example, MO-B catalyst showed 352 (T<sub>IN</sub>), 365 (T<sub>CENTR</sub>) and 346 °C (T<sub>OUT</sub>) at T<sub>SET</sub> = 350 °C and GHSV = 10,000 h<sup>-1</sup>, corresponding to a maximum  $\Delta T$  of 15 °C (Fig. 11d, Table 6). Increasing the GHSV to 50,000 h<sup>-1</sup>,

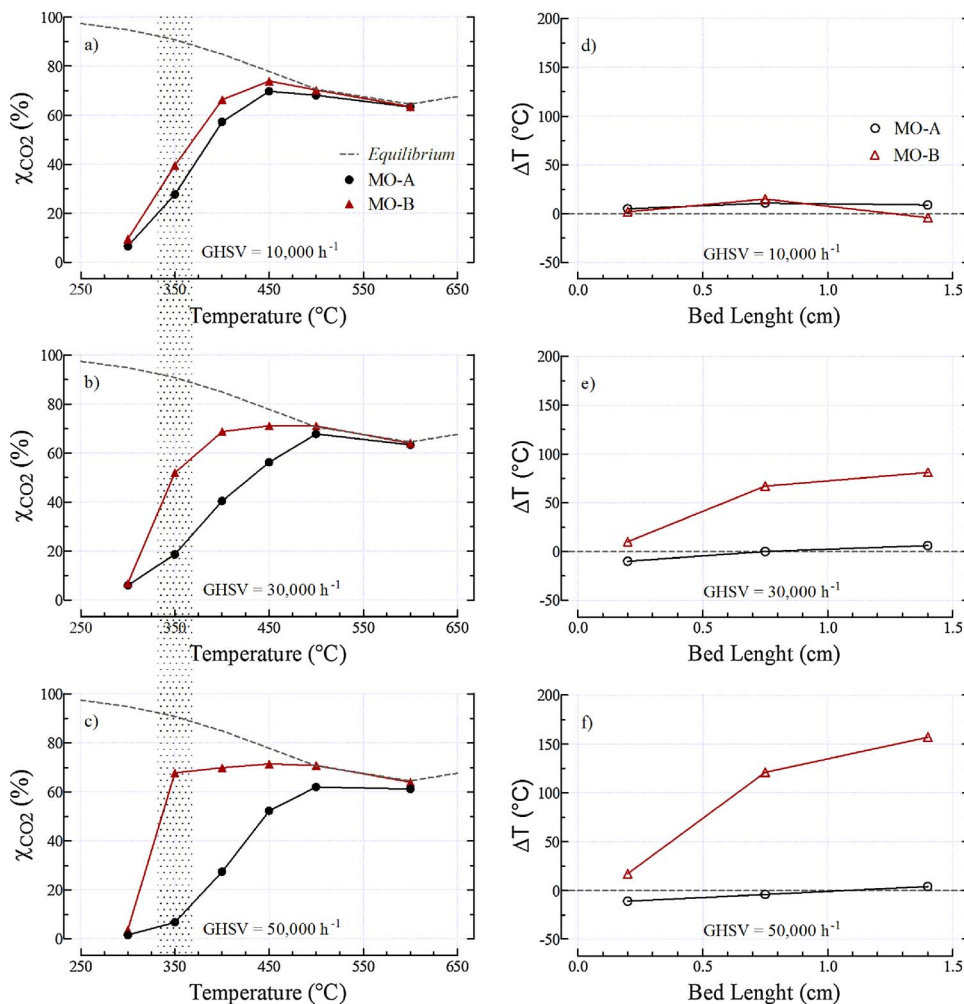


**Fig. 11.** CO<sub>2</sub> methanation activity over structured (MO-A and MO-B) catalysts. Influence of catalytic load (0.2–0.5 g/cm<sup>3</sup>) and set reaction temperature (300–600 °C) on CO<sub>2</sub> conversion at GHSV of 10,000 (a), 30,000 (b) and 50,000 h<sup>-1</sup> (c). Temperature difference ( $\Delta T$ ) between the set temperature ( $T_{SET} = 350$  °C) and the catalyst-bed temperature ( $T_{IN}$ ,  $T_{CENTR}$ ,  $T_{OUT}$ ) at GHSV of 10,000 (d), 30,000 (e) and 50,000 h<sup>-1</sup> (f). Reaction conditions: H<sub>2</sub>/CO<sub>2</sub>/N<sub>2</sub>: 4/1/1 molar, total gas flow: 200–1000 Nml/min.

higher temperatures were recorded as  $T_{IN}$  (367 °C),  $T_{CENTR}$  (471 °C) and  $T_{OUT}$  (507 °C), with a maximum  $\Delta T$  of 157 °C (Fig. 11f, Table 6). Under these conditions, CO<sub>2</sub> conversion increased from ca. 40% to 68% (Fig. 11a–c) by increasing GHSV from 10,000 to 50,000 h<sup>-1</sup>.

Thus, the high activity of the high-load MO-B catalyst led to greater

amounts of reaction heat, that further increased by increasing the reagents flow. The released heat, transferred along the catalytic bed, affected the methanation performance, resulting in an almost flat CO<sub>2</sub> conversion profile in the temperature range 350–600 °C at GHSV of 50,000 h<sup>-1</sup> (Fig. 11c). In addition, the CH<sub>4</sub> concentration increased

**Table 5**

Catalytic activity of structured (MO-A) catalyst for CO<sub>2</sub> methanation. Influence of space velocity (10,000–50,000 h<sup>-1</sup>) and set temperature (300–600 °C) on effluent composition and temperature profile. Reaction conditions: H<sub>2</sub>/CO<sub>2</sub>/N<sub>2</sub>: 4/1/1 molar, total gas flow: 200–1000 Nml/min, catalyst: 0.2 g/cm<sup>3</sup>.

GHSV (h <sup>-1</sup> )	Set temperature (°C)	Effluent composition (%, N <sub>2</sub> -free)					Temperature profile (°C)		
		H <sub>2</sub>	CO <sub>2</sub>	CH <sub>4</sub>	H <sub>2</sub> O	CO	$T_{IN(0.2\text{ cm})}$	$T_{CENTR(0.75\text{ cm})}$	$T_{OUT(1.4\text{ cm})}$
10,000	300	77.4	18.6	1.4	2.6	0.0	300	301	301
	350	65.5	15.4	6.3	12.8	0.0	355	361	359
	400	47.4	10.9	15.8	25.3	0.6	412	418	408
	450	34.5	7.8	19.0	38.1	0.6	467	465	463
	500	36.3	7.8	19.4	35.5	1.0	520	514	492
	600	48.0	7.3	9.5	29.9	5.3	615	610	598
30,000	300	78.4	17.5	0.5	3.6	0.0	293	297	301
	350	75.4	16.4	2.1	5.9	0.2	340	350	356
	400	64.1	12.8	6.7	15.7	0.7	376	405	410
	450	51.5	10.4	12.6	23.2	2.3	416	466	460
	500	42.9	7.9	15.2	31.8	2.2	471	513	486
	600	46.5	7.1	11.5	29.9	5.0	594	612	583
50,000	300	78.2	20.0	0.3	1.5	0.0	291	295	300
	350	75.0	19.1	1.3	4.4	0.2	339	346	354
	400	65.3	15.7	5.0	12.5	1.5	376	403	413
	450	52.4	10.9	9.7	23.6	3.4	410	465	458
	500	47.3	9.0	11.8	27.9	4.0	455	515	480
	600	46.9	7.7	11.1	28.6	5.7	580	616	582

**Table 6**

Catalytic activity of structured (MO-B) catalyst for CO<sub>2</sub> methanation. Influence of space velocity (10,000–50,000 h<sup>-1</sup>) and set temperature (300–600 °C) on effluent composition and temperature profile. Reaction conditions: H<sub>2</sub>/CO<sub>2</sub>/N<sub>2</sub>: 4/1/1 molar, total gas flow: 200–1000 Nml/min, catalyst: 0.5 g/cm<sup>3</sup>.

GHSV (h <sup>-1</sup> )	Set temperature (°C)	Effluent composition (%), N <sub>2</sub> -free)					Temperature profile (°C)		
		H <sub>2</sub>	CO <sub>2</sub>	CH <sub>4</sub>	H <sub>2</sub> O	CO	T <sub>IN(0.2 cm)</sub>	T <sub>CENTR(0.75 cm)</sub>	T <sub>OUT(1.4 cm)</sub>
10,000	300	76.6	16.0	2.3	5.1	0.0	301	305	301
	350	60.0	12.6	10.0	17.4	0.0	352	365	346
	400	37.6	8.1	19.0	35.3	0.0	407	420	379
	450	31.6	6.4	21.6	40.2	0.2	456	462	416
	500	35.2	7.0	19.3	37.8	0.7	510	509	466
	600	51.4	7.0	9.3	27.4	4.9	609	607	587
30,000	300	77.5	18.7	1.2	2.6	0.0	297	303	307
	350	53.7	11.1	11.7	23.5	0.0	360	417	431
	400	40.0	8.4	16.0	35.2	0.4	425	478	447
	450	35.6	7.4	17.6	38.2	1.2	479	512	460
	500	35.6	6.9	17.1	38.9	1.5	530	543	485
	600	47.1	7.5	11.0	29.5	4.9	624	624	588
50,000	300	77.7	19.8	0.8	1.7	0.0	298	306	316
	350	41.1	8.4	15.9	32.8	1.8	367	471	507
	400	35.7	7.5	17.1	37.7	2.0	443	536	512
	450	35.5	7.4	17.5	37.5	2.1	500	550	516
	500	39.3	7.7	15.6	34.8	2.6	544	585	527
	600	46.7	7.7	11.3	28.8	5.5	626	640	60

from 15.9% to 17.5% by increasing temperature from 350 to 450 °C, decreasing afterward to 11.3% at 600 °C, while CO concentration increased to 5.5% at 600 °C, mainly related to the influence of temperature on methanation and RWGS equilibriums (Table 6).

### 3.2.3. Powder and structured catalysts comparison

Powder and structured catalysts were tested by keeping unchanged the volume of catalytic bed (diameter, 1 cm, length, 1.5 cm). However, the MO-B system contained approximately 60% of the catalytic material employed in the packed bed reactor. As reported by Frey et al. [29], a better comparison between powder and monolith could be done considering the CH<sub>4</sub> productivity, expressed as hourly methane produced per unit weight of catalyst (L<sub>CH4</sub>/g h). Fig. 12 compares the CH<sub>4</sub> productivity obtained with powder (50Ni/GDC) and structured (MO-B) catalysts as a function of reaction temperature (T<sub>SET</sub> = 300–600 °C) and space velocity (GHSV = 10,000–50,000 h<sup>-1</sup>).

As expected, MO-B monolith showed higher productivity values than the related 50Ni/GDC sample. High surface-to-volume ratio and good interphase mass transfer of the monolithic systems were able to ensure high methanation activity with low amount of catalytic phase [30,85]. Indeed, higher methane productivity was obtained with the MO-B catalyst (2.5 L<sub>CH4</sub>/g h) than the 50Ni/GDC powder (1.6 L<sub>CH4</sub>/g h). Moreover, the low pressure drops of structured system allowed operating at high space velocity [31,85]. Thus, the CH<sub>4</sub> productivity

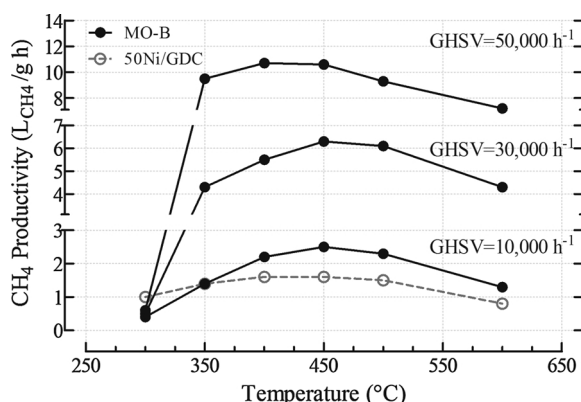


Fig. 12. Effect of set temperature (300–600 °C) and space velocity (10,000–50,000 h<sup>-1</sup>) on CH<sub>4</sub> productivity values over powder (50Ni/GDC) and structured (MO-B) catalysts. Reaction conditions: H<sub>2</sub>/CO<sub>2</sub>/N<sub>2</sub>: 4/1/1 molar, total gas flow: 200–1000 Nml/min.

increased by increasing the space velocity, reaching the highest value (10.7 L<sub>CH4</sub>/g h) at 400 °C and 50,000 h<sup>-1</sup>.

### 3.2.4. Stability test

A long-term test on the MO-B monolith-type structured systems was carried out at T<sub>SET</sub> = 400 °C and GHSV = 30,000 h<sup>-1</sup>, and the results are shown in Fig. 13. Stable performance, both in term of CO<sub>2</sub> conversion (68–69%) and effluent composition over 200 h of time-on-stream, were obtained. Moreover, almost stable temperatures were recorded along the catalytic bed, as reported in Fig. 13. Indeed, T<sub>IN</sub>, T<sub>CENTR</sub> and T<sub>OUT</sub> slightly decreased from 422, 476 and 448 °C (revealed at the beginning of the test) to 417, 468 and 440 °C after 200 h, respectively, confirming the high stability of the studied system.

## 4. Conclusions

CO<sub>2</sub> methanation was investigated over powder and structured Ni/GDC (gadolinium-doped-ceria) catalysts at atmospheric pressure and H<sub>2</sub>/CO<sub>2</sub> = 4 varying temperature (T<sub>SET</sub> = 300–600 °C) and space

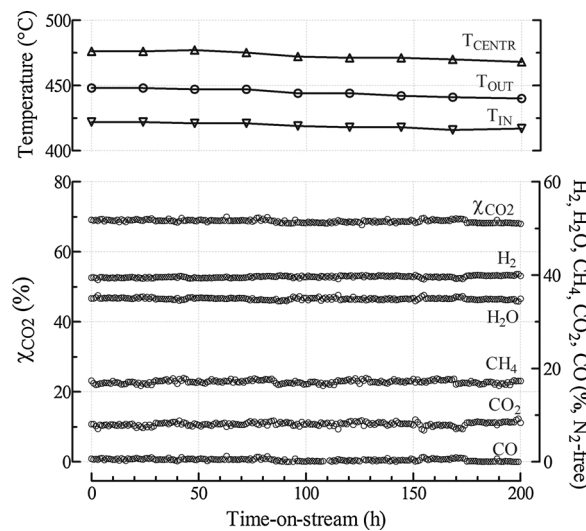


Fig. 13. CO<sub>2</sub> methanation stability of structured (MO-B) catalyst. CO<sub>2</sub> conversion and effluent composition as a function of time-on-stream. Reaction conditions: H<sub>2</sub>/CO<sub>2</sub>/N<sub>2</sub>: 4/1/1 molar, set temperature: 400 °C, GHSV: 30,000 h<sup>-1</sup>, total gas flow: 600 Nml/min, catalyst: 0.5 g/cm<sup>3</sup>.

velocity ( $\text{GHSV} = 10,000\text{-}50,000 \text{ h}^{-1}$ ). Powder systems were synthesized by solution combustion synthesis (SCS) varying the Ni content (15–50 wt.%). The activity increased by increasing the temperature while remaining below the thermodynamic limits, due to the kinetic limitations at relative low temperatures (300–450 °C). A slight decrease in activity was observed further increasing the temperature up to 600 °C, due to thermodynamic limitation of methanation reaction coupled with the occurrence of competitive RWGS equilibrium. Moreover, the activity increased by increasing the Ni loading due to enhanced metal-to-support interaction and moderate-basic sites, as confirmed by  $\text{H}_2\text{-TPR}$  and  $\text{CO}_2\text{-TPD}$  analysis. The presence of  $\text{Ce}^{3+}/\text{Ce}^{4+}$  ion pairs and the surface oxygen vacancies in the GDC support also contributed to enhance the adsorption and activation of  $\text{CO}_2$ .

Monolith-type systems were prepared varying the amount of deposited catalyst on the structured support. It is worth mentioning that the catalyst preparation appeared fully reproducible. Very uniform, thin (10–40 μm) and high-resistance catalytic layers were *in situ* deposited on the cordierite monoliths by the SCS method. Low-loaded monolithic catalyst (0.2 g/cm<sup>3</sup>) showed poor activity, especially at decreased contact time between reactants and catalyst, due to the insufficient amount of catalytic layer. Relative higher activity was recognized using the high-load monolith (0.5 g/cm<sup>3</sup>), closely connected to the temperature profiles recorded on the catalytic bed. High surface-to-volume ratio, good interphase mass transfer and low pressure drops of the structured catalyst led to high methane productivity per unit weight of catalyst. The highest  $\text{CH}_4$  productivity of 10.7 L <sub>$\text{CH}_4$</sub> /g h was obtained at 400 °C and 50,000 h<sup>-1</sup>. Promising long-term stability was observed over 200 h of time-on-stream.

The results presented in this paper provided a platform to further optimization studies of structured catalysts for  $\text{CO}_2$  methanation in power-to-gas applications.

## Acknowledgments

The Authors would like to thank Dr. F. Frusteri for his contribution to the TEM characterization and Dr. L. Spadaro for his contribution to the XPS characterization.

This work was funded by the Italian Ministry of Economic Development in the framework of the “Fondo per la Ricerca di Sistema Elettrico — Piano Triennale 2015–2017 — Progetto Sistemi Elettrochimici per l’accumulo di energia”.

## References

- [1] E.P. Ahern, P. Deane, T. Persson, B.Ó. Gallachóir, J.D. Murphy, A perspective on the potential role of renewable gas in a smart energy island system, *Renew. Energy* 78 (2015) 648–656.
- [2] S. Saeidi, N.A.S. Amin, M.R. Rahimpour, Hydrogenation of  $\text{CO}_2$  to value-added products—A review and potential future developments, *J. CO<sub>2</sub> Util.* 5 (2014) 66–81.
- [3] M.A. Ancona, G. Antonioni, L. Branchini, A. De Pascale, F. Melino, V. Orlandini, V. Antonucci, M. Ferraro, Renewable energy storage system based on a Power-to-Gas conversion process, *Energy Proc.* 101 (2016) 854–861.
- [4] D. Wierzbicki, R. Baran, R. Dębek, M. Motak, T. Grzybek, M.E. Gálvez, P. Da Costa, The influence of nickel content on the performance of hydrotalcite-derived catalysts in  $\text{CO}_2$  methanation reaction, *Int. J. Hydrogen Energy* 42 (2017) 23548–23555.
- [5] G. Cinti, G. Bidini, K. Hemmes, An experimental investigation of fuel assisted electrolysis as a function of fuel and reactant utilization, *Int. J. Hydrogen Energy* 41 (2016) 11857–11867.
- [6] Y. Li, Q. Zhang, R. Chai, G. Zhao, Y. Liu, Y. Lu, Ni-Al<sub>2</sub>O<sub>3</sub>/Ni-foam catalyst with enhanced heat transfer for hydrogenation of  $\text{CO}_2$  to methane, *AIChE J.* 61 (2015) 4323–4331.
- [7] E.A. Quadrelli, K. Armstrong, P. Styring, Potential  $\text{CO}_2$  utilisation contributions to a more carbon-sober future: a 2050 vision, in: P. Styring, E.A. Quadrelli, K. Armstrong (Eds.), *Carbon Dioxide Utilization. Closing the Carbon Cycle*, Elsevier, 2015, pp. 285–302.
- [8] S. Danaci, L. Protasova, J. Lefevere, L. Bedel, R. Guilet, P. Marty, Efficient  $\text{CO}_2$  methanation over Ni/Al<sub>2</sub>O<sub>3</sub> coated structured catalysts, *Catal. Today* 273 (2016) 234–243.
- [9] M.S. Duyar, A. Ramachandran, C. Wang, R.J. Farrauto, Kinetics of  $\text{CO}_2$  methanation over Ru/γ-Al<sub>2</sub>O<sub>3</sub> and implications for renewable energy storage applications, *J. CO<sub>2</sub> Util.* 12 (2015) 27–33.
- [10] R. Daroughi, F. Meshkani, M. Rezaei, Enhanced activity of  $\text{CO}_2$  methanation over mesoporous nanocrystalline Ni/Al<sub>2</sub>O<sub>3</sub> catalysts prepared by ultrasound-assisted co-precipitation method, *Int. J. Hydrogen Energy* 42 (2017) 15115–15125.
- [11] C. Janke, M.S. Duyar, M. Hoskins, R. Farrauto, Catalytic and adsorption studies for the hydrogenation of  $\text{CO}_2$  to methane, *Appl. Catal. B* 152–153 (2014) 184–191.
- [12] J.R. Rostrup-Nielsen, K. Pedersen, J. Sehested, High temperature methanation. Sintering and structure sensitivity, *Appl. Catal. A* 330 (2007) 134–138.
- [13] D. Cui, J. Liu, J. Yu, J. Yue, F. Su, G. Xu, Necessity of moderate metal-support interaction in Ni/Al<sub>2</sub>O<sub>3</sub> for syngas methanation at high temperatures, *RSC Adv.* 5 (2015) 10187–10196.
- [14] D. Pandey, G. Deo, Effect of support on the catalytic activity of supported Ni-Fe catalysts for the  $\text{CO}_2$  methanation reaction, *J. Ind. Eng. Chem.* 33 (2016) 99–107.
- [15] H. Lu, X. Yang, G. Gao, J. Wang, C. Han, X. Liang, C. Li, Y. Li, W. Zhang, X. Chen, Metal (Fe, Co, Ce or La) doped nickel catalyst supported on ZrO<sub>2</sub> modified mesoporous clays for CO and  $\text{CO}_2$  methanation, *Fuel* 183 (2016) 335–344.
- [16] T.A. Le, M.S. Kim, S.H. Lee, T.W. Kim, E.D. Park, CO and  $\text{CO}_2$  methanation over supported Ni catalysts, *Catal. Today* 293–294 (2017) 89–96.
- [17] Y. Xu, Y. Chen, J. Li, J. Zhou, M. Song, X. Zhang, Y. Yin, Improved low-temperature activity of Ni?Ce/γ-Al<sub>2</sub>O<sub>3</sub> catalyst with layer structural precursor prepared by cold plasma for  $\text{CO}_2$  methanation, *Int. J. Hydrogen Energy* 42 (2017) 13085–13091.
- [18] H. Takano, Y. Kirihata, K. Izumiya, N. Kumagai, H. Habazaki, K. Hashimoto, Highly active Ni/Y-doped ZrO<sub>2</sub> catalysts for  $\text{CO}_2$  methanation, *Appl. Surf. Sci.* 388 (2016) 653–663.
- [19] R. Zhou, N. Rui, Z. Fan, C.-J. Liu, Effect of the structure of Ni/TiO<sub>2</sub> catalyst on  $\text{CO}_2$  methanation, *Int. J. Hydrogen Energy* 41 (2016) 22017–22025.
- [20] J. Wang, N. Yao, B. Liu, J. Cen, X. Li, Deposition of carbon species on the surface of metal: as a poison or a promoter for the long-term stability of Ni/SiO<sub>2</sub> methanation catalyst? *Chem. Eng. J.* 322 (2017) 339–345.
- [21] Y. Yu, G.-Q. Jin, Y.-Y. Wang, X.-Y. Guo, Synthetic natural gas from CO hydrogenation over silicon carbide supported nickel catalysts, *Fuel Process. Technol.* 92 (12) (2011) 2293–2298.
- [22] A. Borgschulte, N. Gallandat, B. Probst, R. Suter, E. Callini, D. Ferri, Y. Arroyo, R. Erni, H. Geerlings, A. Zutell, Sorption enhanced  $\text{CO}_2$  methanation, *Phys. Chem. Chem. Phys.* 15 (2013) 9620–9625.
- [23] G. Zhou, H. Liu, K. Cui, A. Jia, G. Hu, Z. Jiao, Y. Liu, X. Zhang, Role of surface Ni and Ce species of Ni/CeO<sub>2</sub> catalyst in  $\text{CO}_2$  methanation, *Appl. Surf. Sci.* 383 (2016) 248–252.
- [24] J. Ashok, M.L. Ang, S. Kawi, Enhanced activity of  $\text{CO}_2$  methanation over Ni/CeO<sub>2</sub>-ZrO<sub>2</sub> catalysts: influence of preparation methods, *Catal. Today* 281 (2017) 304–311.
- [25] S. Tada, T. Shimizu, H. Kameyama, T. Haneda, R. Kikuchi, Ni/CeO<sub>2</sub> catalysts with high  $\text{CO}_2$  methanation activity and high  $\text{CH}_4$  selectivity at low temperatures, *Int. J. Hydrogen Energy* 37 (2012) 5527–5531.
- [26] M. Florea, F. Matei-Rutkovska, G. Postole, A. Urda, F. Neatu, V.I. Pârvulescu, P. Gelin, Doped ceria prepared by precipitation route for steam reforming of methane, *Catal. Today* (2016), <http://dx.doi.org/10.1016/j.cattod.2016.12.006>.
- [27] P. Frontera, A. Macario, G. G. Monforte, M. Bonura, G. Ferraro, V. Dispensa, A.S. Antonucci, P.L. Arićò, The role of Gadolinia Doped Ceria support on the promotion of  $\text{CO}_2$  methanation over Ni and Ni/Fe catalysts, *Int. J. Hydrogen Energy* (2017), <http://dx.doi.org/10.1016/j.ijhydene.2017.09.025>.
- [28] M. Younas, L.L. Kong, M.J.K. Bashir, H. Nadeem, A. Shehzad, S. Sethupathi, Recent advancements, fundamental challenges, and opportunities in catalytic methanation of  $\text{CO}_2$ , *Energy Fuels* 30 (2016) 8815–8831.
- [29] M. Frey, D. Édouard, A.-C. Roger, Optimization of structured cellular foam-based catalysts for low-temperature carbon dioxide methanation in a platelet milli-reactor, *C. R. Chim.* 18 (2015) 283–292.
- [30] V. Tomasić, F. Jović, State-of-the-art in the monolithic catalysts/reactors, *Appl. Catal. A* 311 (2006) 112–121.
- [31] S. Ricca, V. Palma, M. Martino, E. Meloni, Innovative catalyst design for methane steam reforming intensification, *Fuel* 198 (2017) 175–182.
- [32] C. Fukuhara, K. Hayakawa, Y. Suzuki, W. Kawasaki, R. Watanabe, A novel nickel-based structured catalyst for  $\text{CO}_2$  methanation: a honeycomb-type Ni/CeO<sub>2</sub> catalyst to transform greenhouse gas into useful resources, *Appl. Catal. A* 532 (2017) 12–18.
- [33] K.P. Brooks, J. Hu, H. Zhu, R.J. Kee, Methanation of carbon dioxide by hydrogen reduction using the Sabatier process in microchannel reactors, *Chem. Eng. Sci.* 62 (2007) 1161–1170.
- [34] S. Specchia, G. Negro, G. Saracco, V. Specchia, Fuel processor based on syngas production via short contact time catalytic partial oxidation reactors, *Appl. Catal. B* 70 (2007) 525–531.
- [35] S. Specchia, Fuel processing activities at European level: a panoramic overview, *Int. J. Hydrogen Energy* 39 (2014) 17953–17968.
- [36] R. Montanini, F. De Domenico, F. Freni, N. Maugeri, A. Recupero, Structural health monitoring of reinforced concrete beams by means of embedded fiber Bragg grating sensors, *Proc. SPIE 8421, OFS2012 22nd International Conference on Optical Fiber Sensors* (2018), <http://dx.doi.org/10.1117/12.970283>.
- [37] L. Giani, C. Cristiani, G. Groppi, E. Tronconi, Washcoating method for Pd/γ-Al<sub>2</sub>O<sub>3</sub> deposition on metallic foams, *Appl. Catal. B* 62 (2006) 121–131.
- [38] G. Ercolino, S. Karimi, P. Stelmachowski, S. Specchia, Catalytic combustion of residual methane on alumina monoliths and open cell foams coated with Pd/Co<sub>3</sub>O<sub>4</sub>, *Chem. Eng. J.* 326 (2017) 339–349.
- [39] C. Cristiani, C.G. Visconti, E. Finocchio, P.G. Stampino, Pio Forzatti, Towards the rationalization of the washcoating process conditions, *Catal. Today* 147S (2009) S24–S29.
- [40] A. Vita, G. Cristiano, C. Italiano, S. Specchia, F. Cipiti, V. Specchia, Methane oxy-steam reforming reaction: performances of Ru/γ-Al<sub>2</sub>O<sub>3</sub> catalysts loaded on structured cordierite monoliths, *Int. J. Hydrogen Energy* 39 (2014) 18592–18603.
- [41] A. Vita, G. Cristiano, C. Italiano, L. Pino, S. Specchia, Syngas production by methane

- oxy-steam reforming on  $\text{Me}/\text{CeO}_2$  ( $\text{Me} = \text{Rh}, \text{Pt Ni}$ ) catalyst lined on cordierite monoliths, *Appl. Catal. B* 162 (2015) 551–563.
- [42] A. Vita, C. Italiano, C. Fabiano, M. Laganà, L. Pino, Influence of Ce-precursor and fuel on structure and catalytic activity of combustion synthesized  $\text{Ni}/\text{CeO}_2$  catalysts for biogas oxidative steam reforming, *Mater. Chem. Phys.* 163 (2015) 337–347.
- [43] C. Italiano, A. Vita, C. Fabiano, M. Laganà, L. Pino, Bio-hydrogen production by oxidative steam reforming of biogas over nanocrystalline  $\text{Ni}/\text{CeO}_2$  catalysts, *Int. J. Hydrogen Energy* 40 (2015) 11823–11830.
- [44] S. Specchia, C. Galletti, V. Specchia, Solution combustion synthesis as intriguing technique to quickly produce performing catalysts for specific applications, *Stud. Surf. Sci. Catal.* 175 (2010) 59–67.
- [45] A. Vita, C. Italiano, D. Previtali, C. Fabiano, A. Palella, F. Freni, G. Bozzano, L. Pino, F. Manenti, Methanol synthesis from biogas: a thermodynamic analysis, *Renew. Energy* 118 (2018) 673–684.
- [46] J. Xiaoyuan, L. Guanglie, Z. Renxian, M. Jianxin, C. Yu, Z. Xiaoming, Studies of pore structure temperature-programmed reduction performance, and micro-structure of  $\text{CuO}/\text{CeO}_2$  catalysts, *Appl. Surf. Sci.* 173 (2001) 208–220.
- [47] R.K. Singh, A. Shukla, A. Yadav, S. Adak, Z. Iqbal, N. Siddiqui, R. Bal, Energy efficient methane tri-reforming for synthesis gas production over highly coke-resistant nanocrystalline  $\text{Ni-ZrO}_2$  catalyst, *Appl. Energy* 178 (2016) 110–125.
- [48] J. Marrero-Jerez, E. Chinarro, B. Moreno, M.T. Colomer, J.R. Jurado, P. Núñez, TPR studies on  $\text{NiO}-\text{CGO}$  composites prepared by combustion synthesis, *Ceram. Int.* 40 (2014) 3469–3475.
- [49] V.G. Deshmankar, S.L. Owen, R.Y. Abrokwhah, D. Kuila, Mesoporous nanocrystalline  $\text{TiO}_2$  supported metal (Cu, Co, Ni, Pd, Zn, and Sn) catalysts: effect of metal-support interactions on steam reforming of methanol, *J. Mol. Catal. A: Chem.* 408 (2015) 202–213.
- [50] W. Nie, X. Zou, X. Shang, X. Wang, W. Ding, X. Lu,  $\text{CeO}_2$ -assisted Ni nanocatalysts supported on mesoporous  $\gamma\text{-Al}_2\text{O}_3$  for the production of synthetic natural gas, *Fuel* 202 (2017) 135–143.
- [51] M.-Y. Ding, J.-Y. Tu, T.-J. Wang, L.-L. Ma, C.-G. Wang, L.-G. Chen, Bio-syngas methanation towards synthetic natural gas (SNG) over highly active  $\text{Al}_2\text{O}_3-\text{CeO}_2$  supported Ni catalyst, *Fuel Proc. Technol.* 134 (2015) 480–486.
- [52] R.K. Singh, A. Shukla, A. Yadav, L.N.S. Konathala, R. Bal, Effect of metal-support interaction on activity and stability of Ni- $\text{CeO}_2$  catalyst for partial oxidation of methane, *Appl. Catal. B* 202 (2017) 473–788.
- [53] M. Mihet, M.D. Lazar, Methanation of  $\text{CO}_2$  on Ni/ $\gamma\text{-Al}_2\text{O}_3$ : influence of Pt, Pd or Rh promotion, *Catal. Today* (2016), <http://dx.doi.org/10.1016/j.cattod.2016.12.001>.
- [54] M. Nizio, A. Albarazi, S. Cavadias, J. Amouroux, M.E. Galvez, P. Da Costa, Hybrid plasma-catalytic methanation of  $\text{CO}_2$  at low temperature over ceria zirconia supported Ni catalysts, *Int. J. Hydrogen Energy* 41 (2016) 11584–11952.
- [55] P. Kumar, P. With, V.C. Srivastava, R. Gläser, I.M. Mishra, Efficient ceria-zirconium oxide catalyst for carbon dioxide conversions: characterization, catalytic activity and thermodynamic study, *J. Alloys Compd.* 696 (2017) 718–726.
- [56] P. Datta, P. Majewski, F. Aldinger, Study of gadolinia-doped ceria solid electrolyte surface by XPS, *Mater. Charact.* 60 (2009) 138–143.
- [57] F. Arena, R. Di Chio, B. Fazio, C. Espriu, L. Spiccia, A. Palella, L. Spadaro, Probing the functionality of nanostructured MnCeOx catalysts in the carbon dioxide oxidation. Part I. Influence of cerium addition on structure and CO oxidation activity, *Appl. Catal. B* 210 (2017) 14–22.
- [58] F. Arena, C. Italiano, L. Spadaro, Efficiency and reactivity pattern of ceria-based noble metal and transition metal-oxide catalysts in the wet air oxidation of phenol, *Appl. Catal. B* 115–116 (2012) 336–345.
- [59] D. Chen, D. He, J. Lu, L. Zhong, F. Liu, J. Liu, Y. Yu, G. Wan, S. He, Y. Luo, Investigation of the role of surface lattice oxygen and bulk lattice oxygen migration of cerium-based oxygen carriers: XPS and designed H<sub>2</sub>-TPR characterization, *Appl. Catal. B* 218 (2017) 249–259.
- [60] W. Li, X. Nie, X. Jiang, A. Zhang, F. Ding, M. Liu, Z. Liu, X. Guo, C. Song,  $\text{ZrO}_2$  support imparts superior activity and stability of Co catalysts for  $\text{CO}_2$  methanation, *Appl. Catal. B* 220 (2018) 397–408.
- [61] W. Zhen, F. Gao, B. Tian, P. Ding, Y. Deng, Z. Li, H. Gao, G. Lu, Enhancing activity for carbon dioxide methanation by encapsulating (111) facet Ni particle in metal-organic frameworks at low temperature, *J. Catal.* 348 (2017) 200–211.
- [62] Y. Li, X. Wang, C. Song, Spectroscopic characterization and catalytic activity of Rh supported on  $\text{CeO}_2$ -modified  $\text{Al}_2\text{O}_3$  for low-temperature steam reforming of propane, *Catal. Today* 263 (2016) 22–34.
- [63] F. Larachi, J. Pierre, A. Adnot, A. Bernis, Ce 3d XPS study of composite  $\text{Ce}_x\text{Mn}_{1-x}\text{O}_{2-y}$  wet oxidation catalysts, *Appl. Surf. Sci.* 195 (2002) 236–250.
- [64] J. Gao, Y. Wang, Y. Ping, D. Hu, G. Xu, F. Gu, F. Su, A thermodynamic analysis of methanation reactions of carbon oxides for the production of synthetic natural gas, *RSC Adv.* 2 (2012) 2358–2368.
- [65] M.Y.S. Hamid, M.L. Firmansyah, S. Triwahyono, A.A. Jalil, R.R. Mukti, E. Febriyanti, V. Suendo, H.D. Setiabudi, M. Mohamed, W. Nabgan, Oxygen vacancy-rich mesoporous silica KCC-1 for  $\text{CO}_2$  methanation, *Appl. Catal. A* 532 (2017) 86–94.
- [66] L.P. Teh, S. Triwahyono, A.A. Jalil, M.L. Firmansyah, Z.A. Majid, Fibrous silica mesoporous ZSM-5 for carbon monoxide methanation, *Appl. Catal. A* 523 (2016) 200–208.
- [67] M.A.A. Aziz, A.A. Jalil, S. Triwahyono, R.R. Mukti, Y.H. Taufiq-Yap, M.R. Sazegar, Highly active Ni-promoted mesostructured silica nanoparticles for  $\text{CO}_2$  methanation, *Appl. Catal. B* 147 (2014) 359–368.
- [68] L. Xu, H. Yang, M. Chen, F. Wang, D. Nie, L. Qi, X. Lian, H. Chen, M. Wu,  $\text{CO}_2$  methanation over Ca doped ordered mesoporous Ni-Al composite oxide catalysts: the promoting effect of basic modifier, *J.CO<sub>2</sub> Util.* 21 (2017) 200–210.
- [69] K. Stangeland, D.Y. Kalai, H. Li, Z. Yu, Active and stable Ni based catalysts and processes for biogas upgrading: the effect of temperature and initial methane concentration on  $\text{CO}_2$  methanation, *Appl. Energy* (2017), <http://dx.doi.org/10.1016/j.apenergy.2017.08.080>.
- [70] I.A. Fisher, A.T. Bell, A comparative study of CO and  $\text{CO}_2$  hydrogenation over Rh/ $\text{SiO}_2$ , *J. Catal.* 162 (1996) 54–65.
- [71] A. Beuls, C. Swalus, M. Jacquemina, G. Heyen, A. Karelovic, P. Ruiz, Methanation of  $\text{CO}_2$ : further insight into the mechanism over Rh/ $\gamma\text{-Al}_2\text{O}_3$  catalyst, *Appl. Catal. B* 113–114 (2012) 2–10.
- [72] M. Marwood, R. Doepper, A. Renken, In-situ surface and gas phase analysis for kinetic studies under transient conditions. The catalytic hydrogenation of  $\text{CO}_2$ , *Appl. Catal. A* 151 (1997) 223–246.
- [73] A. Westermann, B. Azambre, M.C. Bacariza, I. Graça, M.F. Ribeiro, J.M. Lopes, C. Henriques, Insight into  $\text{CO}_2$  methanation mechanism over NiUSY zeolites: an operando IR study, *Appl. Catal. B* 174–175 (2015) 120–125.
- [74] G.D. Weatherbee, C.H. Bartholomew, Hydrogenation of  $\text{CO}_2$  on group VIII metals: II. Kinetics and mechanism of  $\text{CO}_2$  hydrogenation on nickel, *J. Catal.* 77 (1982) 460–472.
- [75] P.A. Ussa Aldana, F. Ocampo, K. Kobl, B. Louis, F. Thibault-Starzyk, M. Daturi, P. Bazin, S. Thomas, A.C. Roger, Catalytic  $\text{CO}_2$  valorization into  $\text{CH}_4$  on Ni-based ceria-zirconia. Reaction mechanism by operando IR spectroscopy, *Catal. Today* 215 (2013) 201–207.
- [76] Z.A. Ibraeva, N.V. Nekrasov, B.S. Gudkov, V.I. Yakerson, Z.T. Beisembayeva, E.Z. Golosman, S.L. Kiperman, Kinetics of methanation of carbon dioxide on nickel catalyst, *Theor. Exp. Chem.* 26 (1990) 620–624.
- [77] H.Y. Kim, H.M. Lee, J.N. Park, Bifunctional mechanism of  $\text{CO}_2$  methanation on Pd/ $\text{MgO/SiO}_2$  catalyst: independent roles of MgO and Pd on  $\text{CO}_2$  methanation, *J. Phys. Chem. C* 114 (2010) 7128–7131.
- [78] G. Ercolino, P. Stelmachowski, S. Specchia, Catalytic performance of Pd/ $\text{Co}_3\text{O}_4$  on SiC and  $\text{ZrO}_2$  open cell foams for process intensification of methane combustion in lean conditions, *Ind. Eng. Chem. Res.* 56 (2017) 6625–6636.
- [79] F.H. Dekker, A. Bliek, F. Kapteijn, J.A. Moulijn, Analysis of mass and heat transfer in transient experiments over heterogeneous catalysts, *Chem. Eng. Sci.* 50 (1995) 3573–3580.
- [80] J. Kopyscinski, T.J. Schildhauer, F. Vogel, S.M.A. Biollaz, A. Wokaun, Applying spatially resolved concentration and temperature measurements in a catalytic plate reactor for the kinetic study of CO methanation, *J. Catal.* 271 (2010) 262–279.
- [81] E.L. Fornero, J.L. Giombi, D.L. Chiavassa, A.L. Bonivardi, M.A. Baltañas, A versatile Carberry-type microcatalytic reactor for transient and/or continuous flow operation at atmospheric or medium pressure, *Chem. Eng. J.* 264 (2015) 664–671.
- [82] Y. Li, Q. Zhang, R. Chai, G. Zhao, F. Cao, Y. Liu, Y. Lu, Metal-foam-structured  $\text{Ni-Al}_2\text{O}_3$  catalysts: wet chemical etching preparation and syngas methanation performance, *Appl. Catal. A* 510 (2016) 216–226.
- [83] O.P. Klenov, N.A. Chumakova, S.A. Pokrovskaya, A.S. Noskov, Modeling of heat transfer in a porous monolith catalyst with square channels, *Ind. Eng. Chem. Res.* 55 (2016) 3879–3889.
- [84] D. Türks, H. Mena, U. Armbruster, A. Martin, Methanation of  $\text{CO}_2$  on Ni/ $\text{Al}_2\text{O}_3$  in a structured fixed-bed reactor—a scale-up study, *Catal. 7* (2017) 152–167.
- [85] M. Götz, J. Lefebvre, F. Mörs, A.M. Koch, F. Graf, S. Bajohr, R. Reimert, T. Kolb, *Renew. Energy* 85 (2016) 1371–1390.